Original Article

JCBFM

Journal of Cerebral Blood Flow & Metabolism
2021, Vol. 41(7) 1721–1733

DOI: 10.1177/0271678X20963404
journals.sagepub.com/home/jcbfm
SAGE

Evaluation of the potassium channel tracer [^{18}F]3F4AP in rhesus macaques

Nicolas J Guehl[1], Karla M Ramos-Torres[1], Clas Linnman[2], Sung-Hyun Moon[1], Maeva Dhaynaut[1], Moses Q Wilks[1], Paul K Han[1], Chao Ma[1], Ramesh Neelamegam[1], Yu-Peng Zhou[1], Brian Popko[3], John A Correia[1], Daniel S Reich[4], Georges El Fakhri[1], Peter Herscovitch[5], Marc D Normandin[1] and Pedro Brugarolas[1]

Abstract

Demyelination causes slowed or failed neuronal conduction and is a driver of disability in multiple sclerosis and other neurological diseases. Currently, the gold standard for imaging demyelination is MRI, but despite its high spatial resolution and sensitivity to demyelinated lesions, it remains challenging to obtain specific and quantitative measures of molecular changes involved in demyelination. To understand the contribution of demyelination in different diseases and to assess the efficacy of myelin-repair therapies, it is critical to develop new in vivo imaging tools sensitive to changes induced by demyelination. Upon demyelination, axonal K^+ channels, normally located underneath the myelin sheath, become exposed and increase in expression, causing impaired conduction. Here, we investigate the properties of the K^+ channel PET tracer [^{18}F]3F4AP in primates and its sensitivity to a focal brain injury that occurred three years prior to imaging. [^{18}F]3F4AP exhibited favorable properties for brain imaging including high brain penetration, high metabolic stability, high plasma availability, high reproducibility, high specificity, and fast kinetics. [^{18}F]3F4AP showed preferential binding in areas of low myelin content as well as in the previously injured area. Sensitivity of [^{18}F]3F4AP for the focal brain injury was higher than [^{18}F]FDG, [^{11}C]PiB, and [^{11}C]PBR28, and compared favorably to currently used MRI methods.

Keywords

Demyelination, [^{18}F]3F4AP, PET imaging, pharmacokinetics, traumatic brain injury

Received 29 April 2020; Revised 13 August 2020; Accepted 4 September 2020

Introduction

Myelin facilitates rapid propagation of action potentials and provides trophic support and protection to axons.[1] As such, the integrity of the myelin sheath is critical for most brain functions including cognition, visual processing, and ambulation.[2–4] In addition to multiple sclerosis (MS),[5] demyelination is emerging as a prominent cause of disability in many brain diseases including spinal cord injury (SCI),[6] traumatic brain injury (TBI),[7] stroke,[8] and Alzheimer's disease (AD).[9] Currently, demyelination can be detected by histopathology, by PET using tracers that bind to myelin such as [^{11}C]PiB or [^{11}C]MeDAS[10,11] or by MRI.[12,13] Unfortunately, histopathology is not applicable for in

[1]Gordon Center for Medical Imaging, Department of Radiology, Massachusetts General Hospital and Harvard Medical School, Boston, MA, USA
[2]Spaulding Neuroimaging Lab, Spaulding Rehabilitation Hospital and Harvard Medical School, Charlestown, MA, USA
[3]Department of Neurology, Northwestern Feinberg School of Medicine, Chicago, IL, USA
[4]Translational Neuroradiology Section, National Institute of Neurological Disorders and Stroke, National Institutes of Health, Bethesda, MD, USA
[5]Positron Emission Tomography Department, NIH Clinical Center, National Institutes of Health, Bethesda, MD, USA

Corresponding authors:
Pedro Brugarolas, 55 Fruit St., Bulfinch 051, Boston, MA 02114, USA.
Email: pbrugarolas@mgh.harvard.edu

Marc D Normandin, 55 Fruit St., White 427, Boston, MA 02114, USA.
Email: normandin@mgh.harvard.edu

vivo disease monitoring. [^{11}C]PiB and [^{11}C]MeDAS have both been shown to bind to myelin;[10,11] however, these myelin-binding tracers are not ideal due to the high abundance of myelin which can mask small lesions due to spill-in signal from surrounding areas and because of binding to amyloid in the case of [^{11}C]PiB.[14] Finally, while structural and diffusion MRI offer some insight into the structural integrity of white matter, MRI measurements are not specific to white matter lesion properties such as myelin content or fiber density.[15] Furthermore, MRI offers limited sensitivity to gray matter demyelination.[16] Therefore, novel molecular imaging tools for monitoring demyelination in vivo are needed.

A well-established biochemical effect of demyelination that is responsible for the poor conduction of action potentials in demyelinated fibers is the dysregulation of axonal voltage-gated K^+ (K_v) channels.[17] K_v channels are transmembrane proteins that allow the selective passage of K^+ ions across the cell membrane upon membrane depolarization. In the brain, K_v channels are primarily expressed in neurons where they are involved in the propagation of action potentials.[18] In myelinated axons, K_v1.1 and K_v1.2 channels are located near the nodes of Ranvier beneath the myelin sheath.[19] Upon demyelination, these protein channels become exposed to the extracellular milieu, disperse throughout the demyelinated segment and increase in expression several fold resulting in slowed or failed axonal conduction.[17,20,21] This increase in K^+ channel expression upon demyelination has been previously demonstrated by immunohistochemistry in several unrelated models of demyelination including in shiverer mice,[21] lysolecithin-injected rats,[22] cuprizone-fed mice,[23] and experimental autoimmune encephalomyelis (EAE) mice.[24] 4-aminopyridine (4AP) is a blocker of K_v1 channels and is used clinically to enhance conduction of demyelinated fibers.[25,26] This mechanism has been exploited for the symptomatic treatment of MS,[27,28] SCI,[29] and stroke.[30]

3-fluoro-4-aminopyridine, 3F4AP, is a fluorinated analog of 4AP that binds with similar affinity as 4AP to K_v1 channels expressed in *Xenopus* oocytes as well as explanted optic nerves from mice.[31,32] It has been recently shown by autoradiography that [^{14}C]4AP and [^{14}C]3F4AP accumulate in demyelinated areas after intravenous administration in several animal models of demyelination including Shiverer mice, lysolecithin-injected mice, and DTA-mice.[31] This is due to the increased level of expression of K_v1 channels in those areas as well as the increased accessibility of the drug to the channels given the lack of myelin.[20,21,33,34] It has also been reported that 3F4AP can be labeled with fluorine-18[35–37] and that radiofluorinated [^{18}F]3F4AP can be used to detect lysolecithin-induced demyelinated lesions in rat brains using PET.[31] The high sensitivity of this tracer towards demyelination makes it a promising candidate for imaging many neurological diseases where there is demyelination including MS, TBI, SCI, stroke, AD, and others.[34] This tracer also holds promise as a tool for monitoring remyelinating therapies, a major focus in current drug development.[34,38]

In order for a PET tracer to be of clinical value, it must not only bind to a clinically relevant target, it must also have appropriate pharmacokinetics that allow reliable quantification of the target.[39] Ideally, a brain tracer should have high brain penetration, high metabolic stability, high plasma availability, relatively fast kinetics, and high specificity for its target.[39] The goal of this study was to comprehensively evaluate [^{18}F]3F4AP in nonhuman primates in preparation for human studies.

Materials and methods

All experiments involving nonhuman primates were performed in accordance with the U.S. Department of Agriculture (USDA) Animal Welfare Act and Animal Welfare Regulations (Animal Care Blue Book), Code of Federal Regulations (CFR), Title 9, Chapter 1, Subchapter A, Part 2, Subpart C, §2.31. 2017. Experiments were approved by the Animal Care and Use Committee at the Massachusetts General Hospital and the Animal Care and Use Committee at the National Institutes of Health. Animal studies were conducted in compliance with the ARRIVE guidelines (Animal Research: Reporting in Vivo Experiments) for how to report animal experiments.

Study design

The primary objective was to characterize [^{18}F]3F4AP in nonhuman primates. Screening against a panel of 38 other common brain receptors was also performed to rule out off-target binding. [^{18}F]3F4AP whole-body scans were performed on two rhesus macaques (Monkey 1 and Monkey 2) to provide a whole-body dosimetry estimation. In two other rhesus macaques (Monkey 3 and Monkey 4), a total of eight dynamic PET imaging studies with arterial blood sampling were performed to provide a thorough characterization of [^{18}F]3F4AP in vivo pharmacokinetics in the monkey brain. One of the animals (Monkey 4) showed an incidental finding related to a previously sustained focal brain injury and was also scanned with the well-characterized PET tracers [^{11}C]PBR28, [^{11}C]PiB, and [^{18}F]FDG to investigate the nature of the injury. In addition, structural, magnetization transfer, and

diffusion MRI were performed to assess pathological changes. The T1-weighted multi-echo magnetization-prepared rapid gradient-echo (MEMPRAGE) were also used for delineation of brain regions.

Animals and procedures

The animals used in this study were four adult male Rhesus macaques (8–13 years old, 8–17 kg).

Monkey 4 clinical history. Three years prior to imaging and while under a research protocol directed by other investigator, Monkey 4 sustained an accidental injury during a craniotomy procedure. A recording chamber was secured atop the skull and a craniotomy was performed with the intention of later installing an intracranial electrode. Post-procedure monitoring revealed a small dural tear that spread over four weeks. Brain tissue herniated through the torn dura and the recording chamber was explanted and the wound closed without electrodes ever being placed. The animal could not proceed under the original research project without electrodes but appeared to fully recover, and so was subsequently transferred to our imaging protocol under the notion that the injury had left no significant lasting effect.

Preparation of the animals for imaging. Prior to each study, animals were sedated with ketamine/xylazine (10/0.5 mg/kg IM) and were intubated for maintenance anesthesia with isoflurane (1–2% in 100% O_2). A venous catheter was placed for infusion of the radiotracer and, where applicable, an arterial catheter was placed for sampling of the arterial input function. The animal was then positioned on a heating pad on the bed of the scanner for the duration of the study. Additional procedural details are described in the Supplementary Methods (SM).

Receptor panel screen

Samples of non-radiolabeled 4AP and 3F4AP were sent to the psychoactive drug screening program (PDSP) from the National Institutes of Health (NIH) / National Institute of Mental Health (NIMH) at the University of North Carolina.[40] Specific details for each assay can be found in the Assay Protocol Book available on the website: https://pdspdb.unc.edu/pdspWeb/

Radiochemistry

Radiochemical syntheses of [^{18}F]3F4AP, [^{11}C]PBR28, [^{11}C]PiB, and [^{18}F]FDG were performed as previously described.[35,41–43]

Whole-body dynamic PET/CT imaging of rhesus macaques with [^{18}F]3F4AP

Two rhesus macaques (Monkey 1 and Monkey 2) were scanned on a Siemens mCT PET/CT scanner for 4 h as previously described.[31] Procedural details are provided in the SM.

Human radiation dosimetry estimation

Human organ dosimetry estimates were calculated from whole-body dynamic PET data from Monkey 1 and Monkey 2 using OLINDA/EXM software as described in the SM.

Magnetic resonance imaging

Brain MRI was performed on Monkey 3 and Monkey 4 using a 3 T Biograph mMR (Siemens Medical Systems). The following sequences were used MEMPRAGE (pre- and post- Gd), T2-weighted fluid-attenuated inversion recovery (FLAIR), Magnetization Transfer Ratio (MTR), and diffusion tensor imaging (DTI). Acquisition parameters are provided in the SM.

Brain dynamic PET/CT imaging of rhesus macaques with [^{18}F]3F4AP

Dynamic PET/CT imaging (2–3 h) with arterial blood sampling was performed on Monkey 3 and Monkey 4 using a Discovery MI (GE Healthcare). Each animal had two baseline scans which were separated by one month for Monkey 3 and by one year for Monkey 4. Monkey 4 had four other scans with different doses of unlabeled 3F4AP (0.75, 1.25, 2.5, and 4 mg/kg) co-injected with [^{18}F]3F4AP. CT scan was acquired before each PET acquisition for attenuation correction of PET images. See SM for additional details.

Brain PET/CT scans with [^{11}C]PiB, [^{11}C]PBR28, and [^{18}F]FDG

Dynamic PET/CT imaging (90 min) with arterial blood sampling was performed on Monkey 4 after administration of [^{11}C]PiB and [^{11}C]PBR28. Static PET/CT imaging was performed on Monkey 4 1 h after administration of [^{18}F]FDG (6-min scan). Additional details about the procedures and quantification are given in the SM.

Arterial blood sampling

Arterial blood samples of 1–2 mL were drawn every 30 s immediately following radiotracer injection and decreased in frequency to every 30 min toward the end of the scan. [^{18}F]3F4AP metabolism was measured

from blood samples acquired at 5, 10, 15, 30, 60, 90, 120, and up to 180 minutes. An additional blood sample of 3 mL was drawn immediately prior to tracer injection in order to measure the plasma-free fraction f_p of [^{18}F]3F4AP.

Arterial blood processing and radiometabolite analysis

Radioactivity concentration (in kBq/cc) was measured in whole-blood (WB) and subsequently in plasma (PL) following the centrifugation of WB. Radiometabolite analysis was performed using an automated column switching radioHPLC system.[44,45] Additional details are provided in the SM.

Plasma-free fraction determination

Arterial plasma samples of 200 µL drawn before radiotracer injection were spiked with 444 kBq of [^{18}F]3F4AP. Following a 15 min incubation period, radioactive plasma samples were loaded on ultrafiltration tubes (Millipore Centrifree) and centrifuged at 1500*g* for 15 min at room temperature. f_p was calculated as the ratio of free ultrafiltrate to plasma concentration and corrected for binding to the ultrafiltration tube membrane.

Image registration and processing

All PET processing was performed with an in-house developed Matlab software that uses FSL.[46] MR data were processed in native space using FSL. Individual brain MR and PET images were aligned into the MRI NIMH Macaque Template (NMT)[47] and regional time activity curves (TACs) were generated for the occipital cortex, parietal cortex, temporal cortex, frontal cortex, hippocampus, amygdala, striatum, thalamus, white matter, and whole cerebellum. Additional details are provided in the SM.

Quantitative analysis of [^{18}F]3F4AP brain uptake

Regional TACs were analyzed by compartmental modeling using the metabolite-corrected arterial plasma input function. One- (1 T) and two- (2 T) tissue compartment model configurations were investigated while fixing the vascular contribution of the WB radioactivity to the PET measurements to 5%. The 2 T model was also tested in its reversible and irreversible modes. Estimates of the kinetic parameters were obtained using nonlinear weighted least-squares fitting with the weights defined as the frame durations. The regional total volume of distribution (V_T)[48] was calculated as K_1/k_2 for a 1 T compartment model and as $(K_1/k_2) \times (1 + k_3/k_4)$ for a 2 T model (see SM for details on the kinetic parameters). In addition, Logan and multilinear analysis MA1 graphical methods[49,50] for the estimation of V_T was performed. Parametric maps of V_T were generated using the Logan method.

Blinded analysis

Even though the nature of the study did not allow for fully blinded analysis, the investigators evaluating [^{18}F]3F4AP on Monkey 4 were unaware of an injury at the time of data acquisition and analysis.

Statistical analysis

All data are expressed as mean value ± one standard deviation (SD) unless otherwise specified. Agreement between methods was assessed by computing the average measured intraclass correlation coefficient (ICC) among methods or models by use of a two-way mixed-effects model with absolute agreement definition. A p value of 0.05 or less was considered statistically significant. All outliers were included in the analysis, and no data were excluded. The Kolmogorov–Smirnov Test of Normality was used to assess data distribution. Additional details are provided in the SM.

Results

3F4AP does not bind to other common brain receptors with high affinity

The capacity of [^{18}F]3F4AP to bind to brain receptors other than K_v1 channels has not been investigated. For this purpose, we evaluated the binding of 4AP and 3F4AP against 38 common brain targets. The results from this screen are included in Supplementary Table S1. This study showed no significant binding to 37 of the 38 receptors tested and only low affinity binding for histamine H2 receptors (K_i~5 µM).

Whole body dynamic imaging shows organ doses within typical levels for fluorine-18 labeled tracers

In order to estimate the dose of radiation following administration of [^{18}F]3F4AP to human subjects, we calculated the human equivalent doses to the major organs using data from whole body 4-h dynamic scans in two rhesus monkeys (Monkeys 1 and 2). This study showed an effective dose is 21.6 ± 0.6 µSv/MBq, which is comparable to other ^{18}F-labeled tracers (e.g. whole body [^{18}F]FDG effective dose is ~20.0 µSv/MBq[51]) (Table 1).

Table 1. Estimated human organ radiation doses.

Organ	Monkey 1 uGy/MBq	Monkey 2 uGy/MBq	Average uGy/MBq	Std. dev. uGy/MBq
Adrenals	20.0	20.6	20.3	0.4
Brain	16.1	19.4	17.8	2.3
Gallbladder wall	22.5	25.8	24.2	2.3
Small int[a]	21.1	22.2	21.7	0.8
Stomach wall	19.3	29.9	24.6	7.5
Upper LI wall[a]	21.1	20.6	20.9	0.4
Heart wall	17.7	19.9	18.8	1.6
Kidneys	60.4	77.0	68.7	11.7
Liver	27.0	35.1	31.1	5.7
Lungs	12.3	13.5	12.9	0.8
Muscle	15.2	15.2	15.2	0.0
Pancreas	20.4	21.8	21.1	1.0
Red marrow	32.7	21.8	27.3	7.7
Osteogenic cells	46.8	41.7	44.3	3.6
Skin	11.6	11.6	11.6	0.0
Spleen	18.4	27.0	22.7	6.1
Testes	19.9	18.2	19.1	1.2
Thymus	15.8	15.8	15.8	0.0
Thyroid	18.7	18.0	18.4	0.5
Bladder wall	30.6	33.1	31.9	1.8
Whole body	18.6	18.7	18.7	0.1
Effective dose (uSv/MBq)	21.2	22.0	**21.6**	**0.6**

[a]Estimated from whole-body dose.

[^{18}F]3F4AP displays suitable pharmacokinetic properties for PET imaging

Encouraged by prior findings in rodents and primates,[31] the positive dosimetry results, and the apparent low off-target binding, we set out to evaluate the pharmacokinetic properties of [^{18}F]3F4AP in rhesus macaques. [^{18}F]3F4AP was synthesized with high molar activity (>37.0 GBq/μmol) and high radiochemical purity (>98% RCC). The tracer was injected intravenously into two rhesus macaques (Monkey 3 and Monkey 4) and their brains were imaged dynamically for 2–3 h, while arterial blood was sampled for measuring radioactivity concentration time courses in whole blood (WB) and plasma (PL), tracer metabolism as well as plasma-free fraction (f_p).

WB radioactivity time course was consistent across scans and animals (Figure 1(a)). WB to PL radioactivity concentration ratio quickly reached a plateau and was close to unity (WB/PL = 1.05 ± 0.01, Figure 1(b)). Further analysis of the radioactivity in plasma showed a very high f_p ($f_p = 0.92 \pm 0.03$, range: 0.89–0.99) indicating that [^{18}F]3F4AP has minimal binding to plasma proteins. RadioHPLC analysis of selected plasma samples revealed very slow metabolic degradation with only a very small fraction of metabolites (Figure 1(c)) and a very high proportion of parent compound in plasma (>90%) even after 2–3 h post injection (Figure 1(d)). Figure 1(e) shows the average metabolite-corrected arterial plasma curve obtained across scans and animals with the corresponding standard deviation. Taken together, the data in blood indicates high plasma availability, fast plasma clearance, and unusually high metabolic stability, which are ideal properties for PET tracers.

In the brain, [^{18}F]3F4AP peaked quickly (SUV > 3 at ~4 min) and was followed by fast washout. Brain kinetics was fairly homogeneous across brain regions and animals. According to visual inspection of model fits and to the Aikake information criterion (AIC),[52] the preferred model ($AIC_{weight,median} = 0.999$) was a reversible two-tissue compartment model (2T4k) (Figure 2(a) and (b)). K_1 values, reflecting tracer delivery, ranged from ~0.34 mL/min/cc in the white matter to ~0.78 mL/min/cc in the striatum, indicating high brain penetration. The V_T estimated from the 2T4k micro-parameters was robust and the time stability of 2T4k V_T estimates was very good as V_T values estimated using only 60 min of data were in excellent agreement with those obtained using 120 min of PET measurements (mean difference = −0.05 ± 0.10 mL/cc, average intraclass correlation coefficient (ICC) = 0.965

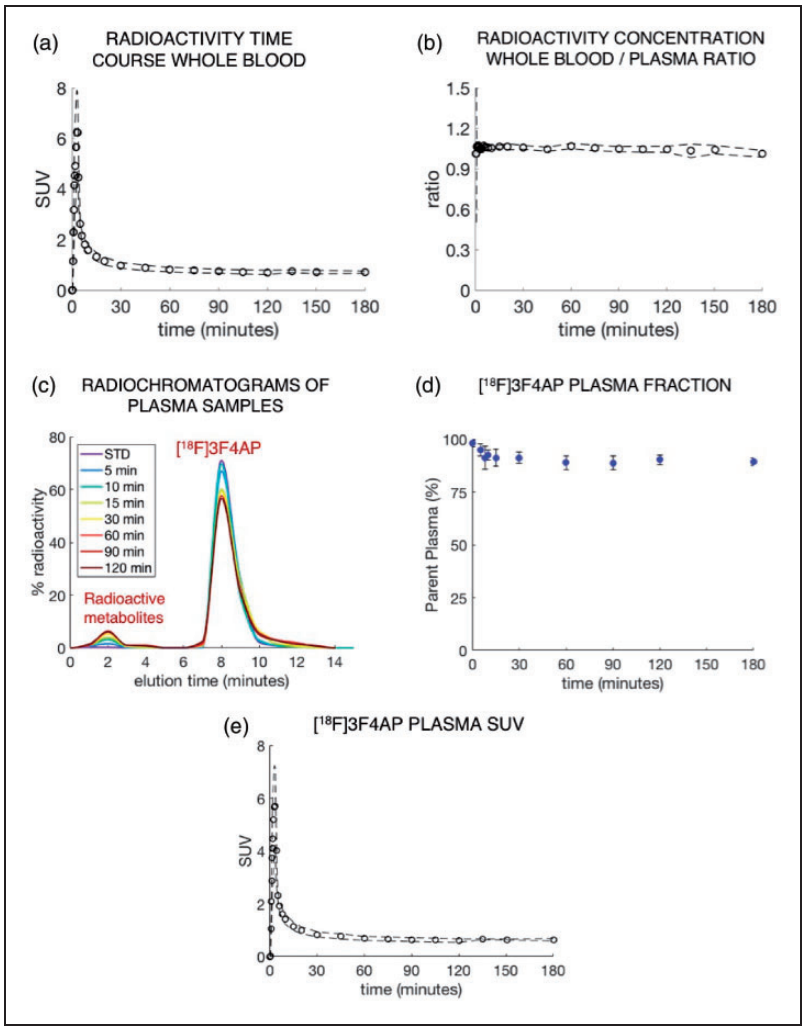

Figure 1. Characterization of [^{18}F]3F4AP in blood. (a) Whole-blood SUV time course. (b) Whole-blood to plasma radioactivity concentration ratio. (c) RadioHPLC chromatogram of plasma samples from a representative study. (d) Time course of remaining parent compound in plasma. (e) Metabolite-corrected [^{18}F]3F4AP SUV time course in plasma. (Plots a, b, d, and e show mean $\pm$ s.d. across animals (N = 2) and scans (2 in Monkey #3 and 6 in Monkey #4). Plot c shows data for a representative study).

with a 95% confidence interval (CI95%) of [0.916, 0.982]). V_T was higher in cortical regions than in the white matter as previously described (Figure 3). High signal was observed in the pituitary gland and sinuses in Monkey 3, which deserves future investigation. In terms of reproducibility, V_T values were consistent in both animals and showed low variability across all baseline scans with a coefficient of variation (COV) within 10% for all brain regions surveyed in this work (mean COV = 5.96 $\pm$ 2.07%, Supplementary Table S2). Finally, blood-based Logan plots (Figure 2 (c) and (d)) linearized very well for all datasets by a 30 min t^* and estimated V_T values were in good agreement with those obtained from the full compartment analysis (2T4k) (mean difference = -0.05 ± 0.07 mL/cc, average measure ICC = 0.976 with CI95% of [0.920, 0.989]). Similar agreement was observed between V_T estimates obtained from MA1 and those obtained from the 2T4k model (mean difference = -0.05 ± 0.07 mL/cc, average measure ICC = 0.973 with CI95% of [0.919,0.987]).

Finally, motivated by the high metabolic stability of 3F4AP and the stable WB to PL radioactivity concentration ratio, we investigated the use of an image derived input function (IDIF) in lieu of using arterial blood sampling to derive the model input function (IF) for quantification of V_T. The IDIF was extracted from a region-of-interest (ROI) positioned in the left ventricular chamber of the heart (Supplementary Figure S1). Visually, the obtained image-derived PL curves were in very good agreement with those obtained from arterial blood sampling (Supplementary Figure S2) and the area under the curve (AUC) was similar (mean

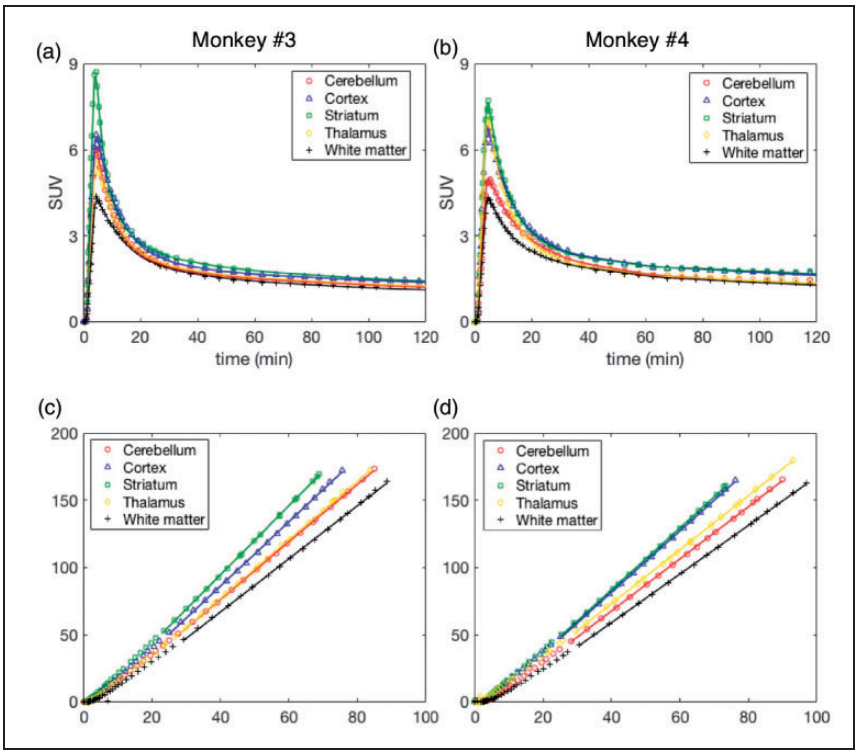

Figure 2. [^{18}F]3F4AP kinetics in different brain regions of Monkeys 3 and 4. (a and b) Time-activity curves and 2T4k model fits. (c and d) Logan plots using a 30 min t^* and corresponding to brain time-activity curves shown in a and b. a and c show data acquired from Monkey 3, while b and d are from Monkey 4. For each monkey, data shown correspond to a single baseline study.

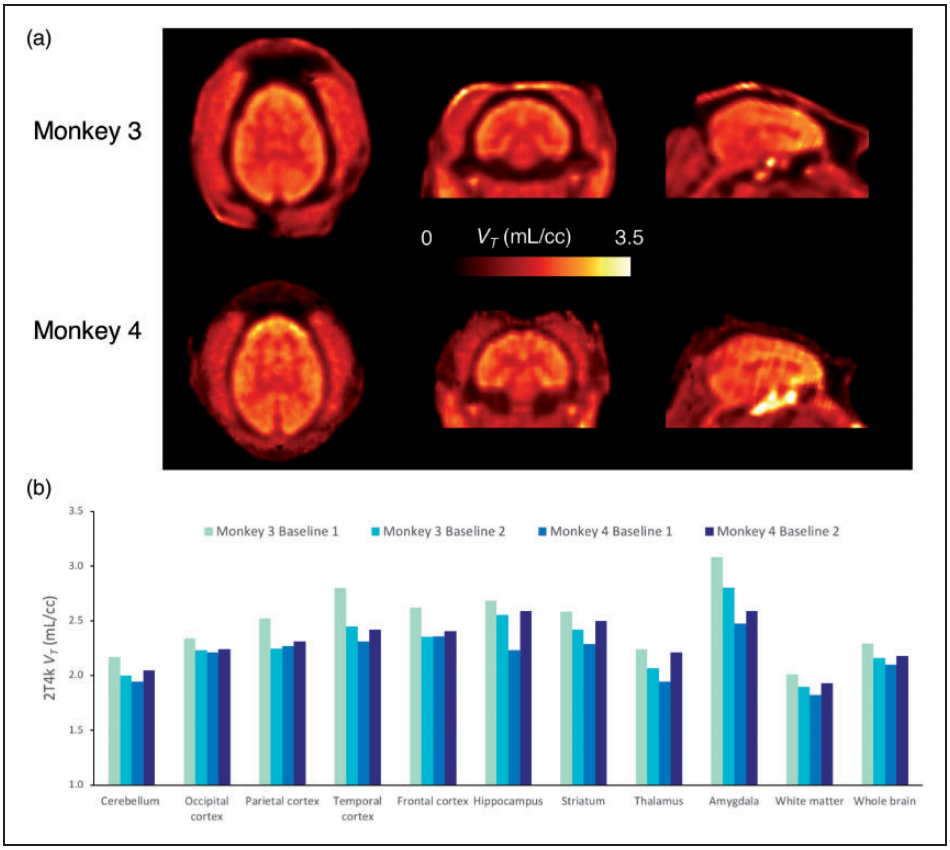

Figure 3. [^{18}F]3F4AP in the monkey brain. (a) Representative parametric images of Monkey 3 and Monkey 4. Hotspot below the brain corresponds to the pituitary gland and ethmoid sinuses. (b) Regional 2T4k V_T values for each baseline scans and each animal.

difference = 4.9 ± 0.1%). Consequently, the quantification demonstrated a good agreement in V_T values (mean difference = −0.06 ± 0.07 mL/cc, average measure ICC = 0.963 with CI95% of [0.797, 0.988]).

It is ineffective to block [^{18}F]3F4AP signal with unlabeled 3F4AP

Given the low lipophilicity of 3F4AP (logD at pH 7.4 = 0.41) and the negligible off-target binding in brain tissue slices previously reported,[31] we hypothesized that the [^{18}F]3F4AP signal measured in the brain reflects tracer binding to K^+ channels as well as a nondisplaceable component that mostly reflects free tracer in the intra and extracellular spaces. In order to confirm this hypothesis, we attempted to block the specific signal using unlabeled 3F4AP. For this purpose, we performed four scans in Monkey 4 while coinjecting the tracer with nonradiolabeled 3F4AP at doses ranging from 0.75 to 4 mg/kg. The highest dose tested (4 mg/kg) caused moderate physiological changes including increased heart rate (from 80 to 93 bpm) and increased mean blood pressure (from 55 to 69 mmHg). Furthermore, when the animal arose from anesthesia, it was observed to be shivering, which occurs with K^+ channel blockers prior to seizures.[53] In mice, 3F4AP as well as 4AP caused tremors at ~6 mg/kg (i.p.) and seizures at ~10 mg/kg.[31] At the doses tested, no obvious blocking (assessed by reduction in V_T) was observed (Supplementary Table S3), likely because the doses were below the dose required to saturate the receptors. In fact, an increase in V_T greater than the test/retest variability was observed with increasing doses of 3F4AP which could be due to more channels transitioning to the open state (bindable conformation) upon co-injection of unlabeled 3F4AP (see Discussion).

[^{18}F]3F4AP shows high sensitivity to a focal brain injury

Monkey 4 showed a focal hotspot in a small focal area of the right frontal cortex. The locus of enhanced uptake corresponded to the site of a minor intracranial injury sustained during a craniotomy procedure three years prior to imaging, and was consistent with the burr hole seen on the CT (Figure 4(a)). Moreover, the TAC demonstrated very distinct pharmacokinetics with characteristics consistent with increased binding (Figure 4(b)). Quantitative analysis showed a 40.3 ± 14.4% (N = 6 scans) higher V_T in the injury site compared to the contralateral site which could not be attributed to changes in perfusion since the quantitative analysis actually demonstrated a lower K_1 value (−59.4 ± 10.8%) in this focal spot compared to contralateral site. For comparison, the same analysis was also performed on Monkey 3, which did not undergo a craniotomy and revealed no differences in V_T or K_1.

To further investigate the nature of the injury and the potential underlying mechanisms driving [^{18}F]3F4AP signal, we performed additional PET scans with [^{18}F]FDG, [^{11}C]PBR28, and [^{11}C]PiB as well as MRI with myelin-specific sequences. [^{18}F]FDG was selected to assess tissue metabolism, confirm the presence of living tissue in the affected area, and rule out potential processes that could lead to general increase in tracer uptake. [^{11}C]PBR28 (TSPO tracer) was selected to assess inflammation,[54,55] and [^{11}C]PiB was selected to assess demyelination[10,56,57] and rule out the presence of amyloid[14,58] (although this was not suspected). In addition, MRI sequences included MEMPRAGE, FLAIR, MTR, and DTI as they can inform of demyelination and other pathologies such as lesion burden and atrophy.[59–61] Images obtained from the different PET tracers and MR sequences are

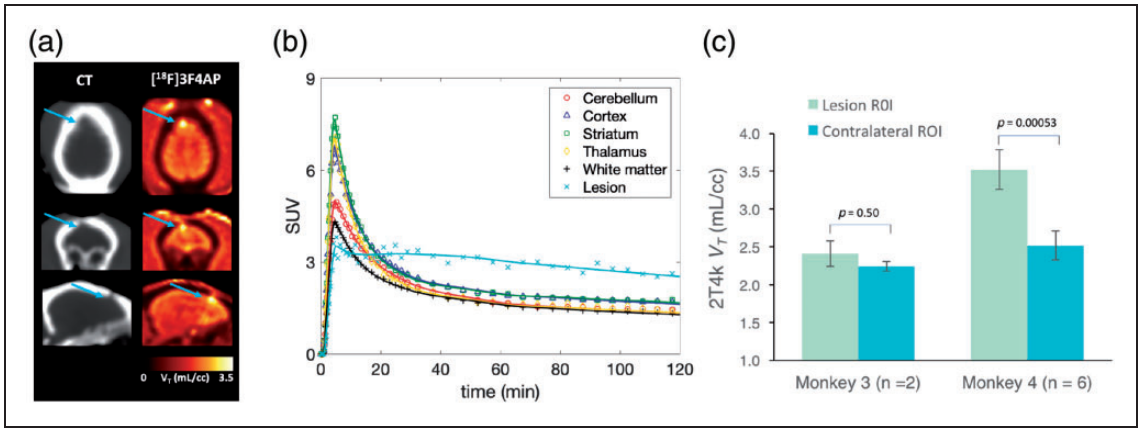

Figure 4. Evaluation of [^{18}F]3F4AP in a focal brain injury. (a) CT and [^{18}F]3F4AP PET images of Monkey 4. Arrow points to the location of the injury. (b) Time-activity curve from the lesion (light blue) of Monkey 4 showing very distinct pharmacokinetic as compared to other brain regions. (c) 2T4k V_T in lesion was significantly higher than V_T in contralateral site. For comparison, the other animal showed no differences in corresponding brain regions.

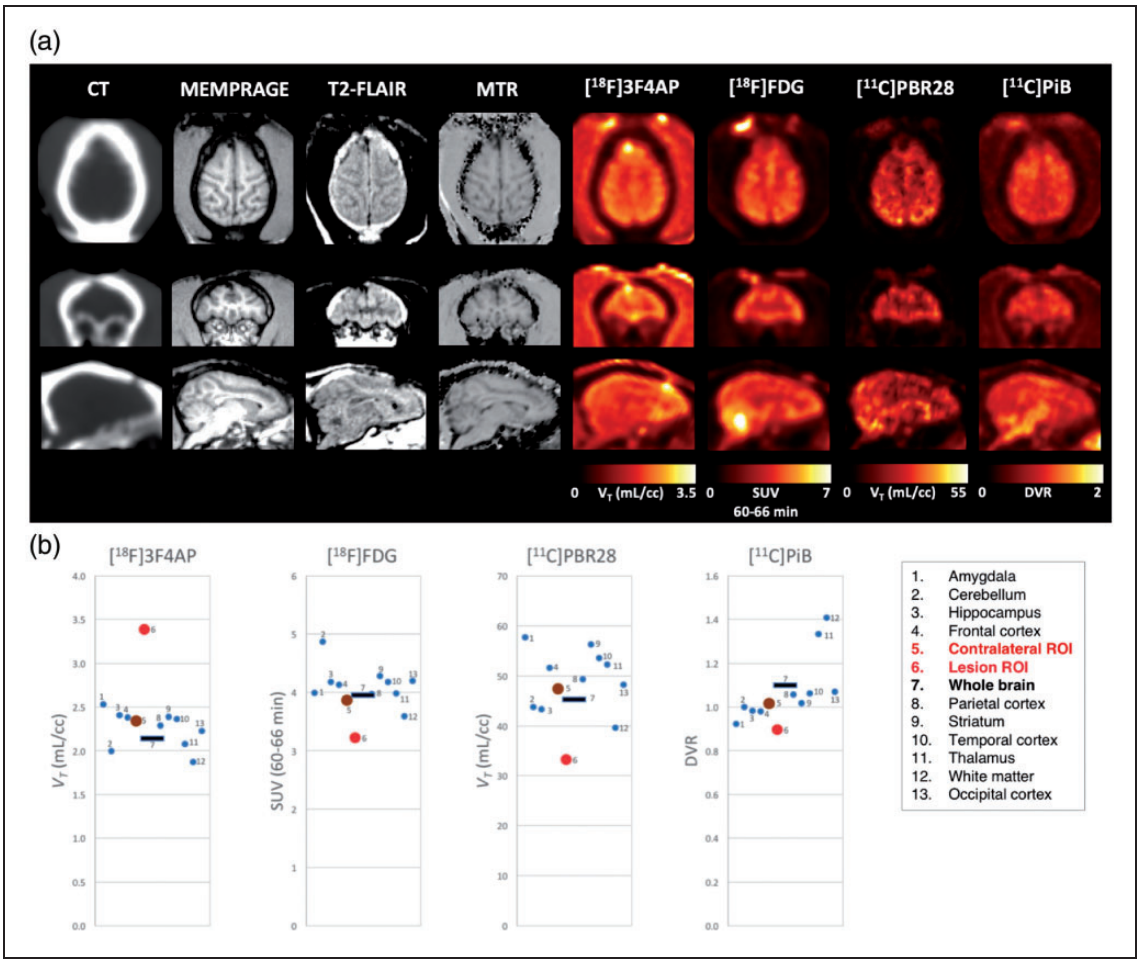

Figure 5. Comparison of [^{18}F]3F4AP with other PET radiotracers and imaging modalities. (a) CT, MRI (MEMPRAGE, T2-FLAIR, and MTR) and parametric PET images ([^{18}F]3F4AP, [^{18}F]FDG [^{11}C]PBR28, and [^{11}C]PiB) of Monkey 4. (b) Brain regional values of the different brain PET tracers.

shown in Figure 5 and zoomed on the lesion in Supplementary Figure S3. Qualitatively, [^{18}F]3F4AP appeared more sensitive for detecting the lesion than any other imaging methods tested. Quantitatively, ROI-based analysis of the [^{18}F]3F4AP images showed the V_T value for lesion to be 5.7 standard deviations higher than the mean V_T of all normal brain regions (Figure 5(b)). In comparison, [^{18}F]FDG showed a −18% reduction in $SUV_{60–66min}$ in the lesion compared to the contralateral ROI which corresponds to 3.0 standard deviations of the $SUV_{60–66min}$ values of all other brain regions (Figure 5(b)). The changes in [^{18}F]FDG uptake were suggestive of hypoperfusion and/or hypometabolism ruling out processes that could result in a general increase in tracer binding. In the case of [^{11}C]PBR28, the V_T in the lesion was −29.9% lower than the contralateral side, which corresponds to 2.85 standard deviations of the V_T of all other brain regions (Figure 5(b)). Furthermore, kinetic analysis of [^{11}C]PBR28 showed a −55.1% reduction in K_1 in the lesion compared to contralateral ROI. The changes observed with [^{11}C]PBR28 indicated reduced perfusion and no discernible inflammation. In the case of [^{11}C]PiB, there was a −11.9% decrease in DVR in the lesion compared to the contralateral ROI which corresponds to 1.24 standard deviations of the DVR values of all other brain regions (Figure 5(b)). The changes in [^{11}C]PiB indicated that there was no amyloid accumulation in the lesion area and suggest possible demyelination.

Results from the quantitative analysis of the MRI data comparing the mean voxel intensity in the lesion to the contralateral mirror ROI are provided in Supplementary Table S4. This analysis showed a modest decrease in MEMPRAGE signal (−9% with Cohens $d = 0.58$) as well as T2-FLAIR (−14% with Cohens $d = 0.58$) and MTR (−15% with Cohens $d = 1.28$). There were also small changes on DTI

measures that displayed a trend in altered diffusion properties (mean diffusivity and axial diffusivity, $p = 0.10$ and $p = 0.05$). In addition, no gadolinium contrast enhancement was seen in the lesion. Changes on the MRI were indicative of an intact blood–brain barrier, gliosis, and encephalomalacia with possible demyelination. For completeness, the same voxel-based analyses were performed on the PET parametric images ([^{18}F]3F4AP, [^{11}C]PBR28, [^{11}C]PiB, and [^{18}F]FDG) and the results are also included in Supplementary Table S4.

Discussion

When an area of the brain is injured by an autoimmune attack, a physical blow, a transient lack of oxygen or other insult, one consequence is damage to oligodendrocytes and myelin. Such damage to the myelin sheath hampers the ability of neurons to propagate action potentials, which can cause a myriad of symptoms ranging from cognitive deficits to physical disability.[5] Given that demyelination is potentially reversible and that it is one of the drivers of disability in MS and likely in many other diseases, it is of utmost importance to develop methods to detect demyelination and monitor remyelination.

Currently, demyelination is primarily imaged using MRI. Even though MRI is highly sensitive to demyelinated lesions in the white matter, it lacks specificity as many potentially coexisting pathological processes such as inflammation or axonal loss may result in similar findings. Furthermore, the sensitivity of MRI to gray matter demyelination is low.[16] PET, on the other hand, provides quantitative and biochemically specific information that can complement MRI findings. Previous approaches to image demyelination with PET involved the use of ligands that bind to myelin,[10,11] which present several limitations including a narrow dynamic range of the measured signal and spill-in signal from adjacent areas due to the limited resolution of PET. Recently, we developed [^{18}F]3F4AP, a PET radioligand that binds to K_v1 channels and demonstrated that it preferentially localizes to demyelinated lesions in several rodent models of demyelination and readily penetrates the blood–brain barrier of primates.[31] Targeting K^+ channels is an indirect method to image demyelination and direct proof showing increases in K^+ expression or accessibility in areas of increased tracer binding has not yet been published. However, there is strong evidence that $K_v1.1$ and $K_v1.2$ increase in expression[17,20–24] and accessibility[33] upon demyelination and that [^{18}F]3F4AP can bind to these channels.[31,32] In view of these promising findings, the primary purpose of the present study was to conduct a thorough evaluation of [^{18}F]3F4AP in nonhuman primates including whole-body radiation dosimetry, evaluation of binding to other receptors, and pharmacokinetic modeling.

This present work demonstrates that [^{18}F]3F4AP possesses very good properties as a PET radiotracer including negligible binding to other common brain receptors (Sup. Table 1), low radiation doses (Table 1), high metabolic stability, low plasma protein binding, and suitable kinetics in plasma (Figure 1) and brain (Figure 2). [^{18}F]3F4AP kinetics in the brain were best described using a reversible two-tissue compartment model with a fixed vascular contribution, which provided a robust quantification of [^{18}F]3F4AP signal using the total volume of distribution V_T as the outcome measure.

These favorable properties resulted in high repeatability and time stability of V_T estimates as well as low intersubject variability (Figure 3). In two studies for which we had both the monkey's heart and brain in the field of view (FOV), we were able to obtain an accurate IDIF from a ROI positioned in the left ventricular chamber (Supplementary Figures S1 and S2), which suggests that [^{18}F]3F4AP signal may be accurately quantified using standard kinetic modeling methods without the invasive procedure of arterial cannulation.

Our findings also show that it is ineffective to block [^{18}F]3F4AP signal using unlabeled 3F4AP. Since excessive blockade of K^+ channels causes seizures,[53] we gradually increased the dose to the highest dose that we estimated would not cause seizures. We had hypothesized that as K^+ channels become occupied by the unlabeled 3F4AP, there would be a lower number of available channels for the radiotracer to bind and, consequently, we would observe a reduction in V_T. Nevertheless, higher V_T values were observed upon coinjection of unlabeled 3F4AP (Supplementary Table S2). Upon further examination of this phenomenon, we found a previous report showing that application of high dose of 4AP onto the pial surface of rats caused a local increase in [^{3}H]4AP binding due to seizure spreading.[62] This finding leads us to propose a mechanism by which as the concentration of 4AP (or 3F4AP) increases, neuronal firing also increases, which results in more channels in the open, bindable, conformation[63] leading to an overall increase in binding.

Interestingly, we incidentally observed enhanced [^{18}F]3F4AP uptake at the site of a focal intracranial injury sustained during a surgical procedure three years prior to imaging (Figure 4). We subsequently performed advanced MRI to assess myelin in the region and scanned the animal with tracers for glucose metabolism, [^{18}F]FDG, microglial activation, [^{11}C]PBR28, and amyloid/myelin, [^{11}C]PiB (Figure 5). This comparative study revealed hypoperfusion in the

lesion area with no inflammation or amyloid accumulation. Furthermore, the [^{11}C]PiB scan was suggestive of demyelination. From the tracers studied, 3F4AP was the only tracer that showed an increased binding in the injury, and it was also the tracer with the highest apparent sensitivity (Figure 5). On the MRI, some of the measures showed clear differences between the lesion and contralateral side (Supplementary Table S3). For example, MTR, which is commonly interpreted as a marker of myelination,[64] showed significant decrease in the lesion. However, other MRI measures such as T2-FLAIR and MEMPRAGE showed changes that are not typically seen in demyelinated lesions. Taken together, MRI findings showed an intact blood–brain barrier, gliosis, encephalomalacia, and possible demyelination. The apparent inconsistency in measures of demyelination may arise from the difficulty of detecting cortical demyelination using conventional MRI[16] or from upregulation of K^+ channels through a mechanism independent of demyelination. For example, although the negative [^{11}C]PBR28 results suggest that there were no activated microglia in the injury, it is known that microglia express $K_v1.3$[65] which could potentially lead to increased tracer binding. Therefore, it will be important to examine via histopathology when the animal reaches the end of its life whether the K^+ channels in the injury site are from demyelinated axons or from other neuronal structures or cell types. In addition, although current evidence suggests that demyelinated axons are the primary target of [^{18}F]3F4AP, future human studies should examine the possibility that K_v channels expressed in other cells may contribute signal.

In summary, this study supports the conclusion that [^{18}F]3F4AP is a promising PET radiotracer for imaging voltage-gated K^+ channels in demyelination, showcases the potential of [^{18}F]3F4AP for detecting chronic brain injuries, and warrants further investigation in humans.

Funding

The author(s) disclosed receipt of the following financial support for the research, authorship, and/or publication of this article: This study was partially supported by the following grants: R00EB020075 (PB), R01NS114066 (PB), P41EB022544 (MDN), S10OD018035 (GEF and MDN), T32EB013180 (GEF), Philippe Foundation award (NJG), Intramural Research Program of NINDS (DSR), Ellen R. and Melvin J. Gordon Center for the Cure and Treatment of Paralysis (CL), The Polsky Center for Innovation and Entrepreneurship at the University of Chicago (BP and PB). Adelson Medical Research Foundation (DSR, BP).

Acknowledgements

We thank Daniel Yokell at the MGH Gordon PET Radiopharmacy for providing [^{18}F]FDG and [^{11}C]PiB, David Lee and Timothy Beaudoin at the MGH Gordon PET Cyclotron for producing ^{18}F and ^{11}C for the synthesis of [^{18}F]3F4AP and [^{11}C]PBR28. We thank the veterinary staff (Helen Deng and Eric McDonald) for assistance with animal handling.

Declaration of conflicting interests

The author(s) declared the following potential conflicts of interest with respect to the research, authorship, and/or publication of this article: PB and BP are named coinventors on patents concerning [^{18}F]3F4AP. All other authors declare no conflicts of interest related to this work.

Authors' contributions

NJG: processed and analyzed the brain PET imaging data and blood data, KMRT: synthesized [^{18}F]3F4AP for most of the studies, CL: analyzed the MRI data, MD: processed the blood samples, SHM: performed plasma radioHPLC analysis, MQW: assisted with FDG and MRI scans, PKH and CM: performed the MRI scans, RN: implemented [^{18}F]3F4AP synthesis method and synthesized [^{11}C]PBR28, YPZ: assisted with the synthesis of [^{11}C]PBR28, JAC: performed dosimetry calculations, BP: contributed to the dosimetry study and interpretation of the findings, DSR: contributed to MR interpretation, GEF: contributed to the brain imaging study and data interpretation, PH: performed whole body PET scans, MDN: contributed to the study design, performed monkey brain PET scans and supervised the processing and analysis of PET data, PB: conceived the project, contributed to the study design, the synthesis of [^{18}F]3F4AP and supervised the entire project. NJG and PB wrote the manuscript and all authors reviewed and approved it.

ORCID iD

Pedro Brugarolas https://orcid.org/0000-0002-7455-2743

Supplementary material and data availability

Supplemental material for this article is available online. The datasets generated and/or analyzed during the current study are available from the corresponding author on reasonable request.

References

1. Nave KA. Myelination and the trophic support of long axons. *Nat Rev Neurosci* 2010; 11: 275–283.
2. Fields RD. White matter in learning, cognition and psychiatric disorders. *Trends Neurosci* 2008; 31: 361–370.
3. Etxeberria A, Hokanson KC, Dao DQ, et al. Dynamic modulation of myelination in response to visual stimuli alters optic nerve conduction velocity. *J Neurosci* 2016; 36: 6937–6948.

4. Tranchant C, Bhatia KP and Marsden CD. Movement disorders in multiple sclerosis. *Mov Disord* 1995; 10: 418–423.
5. Reich DS, Lucchinetti CF and Calabresi PA. Multiple sclerosis. *N Engl J Med* 2018; 378: 169–180.
6. Waxman SG. Demyelination in spinal cord injury. *J Neurol Sci* 1989; 91: 1–14.
7. Armstrong RC, Mierzwa AJ, Marion CM, et al. White matter involvement after TBI: clues to axon and myelin repair capacity. *Exp Neurol* 2016; 275(Pt 3): 328–333.
8. Aboul-Enein F, Rauschka H, Kornek B, et al. Preferential loss of myelin-associated glycoprotein reflects hypoxia-like white matter damage in stroke and inflammatory brain diseases. *J Neuropathol Exp Neurol* 2003; 62: 25–33.
9. Ihara M, Polvikoski TM, Hall R, et al. Quantification of myelin loss in frontal lobe white matter in vascular dementia, Alzheimer's disease, and dementia with Lewy bodies. *Acta Neuropathol* 2010; 119: 579–589.
10. Bodini B and Stankoff B. Imaging central nervous system demyelination and remyelination by positron-emission tomography. *Brain Plast* 2016; 2: 93–98.
11. Wu C, Wang C, Popescu DC, et al. A novel PET marker for in vivo quantification of myelination. *Bioorg Med Chem* 2010; 18: 8592–8599.
12. Tillema JM and Pirko I. Neuroradiological evaluation of demyelinating disease. *Ther Adv Neurol Disord* 2013; 6: 249–268.
13. Heath F, Hurley SA, Johansen-Berg H, et al. Advances in noninvasive myelin imaging. *Dev Neurobiol* 2018; 78: 136–151.
14. Klunk WE, Engler H, Nordberg A, et al. Imaging brain amyloid in Alzheimer's disease with Pittsburgh compound-B. *Ann Neurol* 2004; 55: 306–319.
15. Filippi M and Rocca MA. MR imaging of multiple sclerosis. *Radiology* 2011; 259: 659–681.
16. Fox RJ, Beall E, Bhattacharyya P, et al. Advanced MRI in multiple sclerosis: current status and future challenges. *Neurol Clin* 2011; 29: 357–380.
17. Coman I, Aigrot MS, Seilhean D, et al. Nodal, paranodal and juxtaparanodal axonal proteins during demyelination and remyelination in multiple sclerosis. *Brain* 2006; 129: 3186–3195.
18. Trimmer JS and Rhodes KJ. Localization of voltage-gated ion channels in mammalian brain. *Annu Rev Physiol* 2004; 66: 477–519.
19. Waxman SG and Ritchie JM. Molecular dissection of the myelinated axon. *Ann Neurol* 1993; 33: 121–136.
20. Arroyo EJ, Sirkowski EE, Chitale R, et al. Acute demyelination disrupts the molecular organization of peripheral nervous system nodes. *J Comp Neurol* 2004; 479: 424–434.
21. Sinha K, Karimi-Abdolrezaee S, Velumian AA, et al. Functional changes in genetically dysmyelinated spinal cord axons of shiverer mice: role of juxtaparanodal K_v1 family K^+ channels. *J Neurophysiol* 2006; 95: 1683–1695.
22. Rasband MN, Trimmer JS, Schwarz TL, et al. Potassium channel distribution, clustering, and function in remyelinating rat axons. *J Neurosci* 1998; 18: 36–47.
23. Bagchi B, Al-Sabi A, Kaza S, et al. Disruption of myelin leads to ectopic expression of K(V)1.1 channels with abnormal conductivity of optic nerve axons in a cuprizone-induced model of demyelination. *PLoS One* 2014; 9: e87736.
24. Jukkola PI, Lovett-Racke AE, Zamvil SS, et al. K^+ channel alterations in the progression of experimental autoimmune encephalomyelitis. *Neurobiol Dis* 2012; 47: 280–293.
25. Gutman GA, Chandy KG, Grissmer S, et al. International union of pharmacology. LIII. Nomenclature and molecular relationships of voltage-gated potassium channels. *Pharmacol Rev* 2005; 57: 473–508.
26. Sherratt RM, Bostock H and Sears TA. Effects of 4-aminopyridine on normal and demyelinated mammalian nerve fibres. *Nature* 1980; 283: 570–572.
27. Stefoski D, Davis FA, Faut M, et al. 4-Aminopyridine improves clinical signs in multiple sclerosis. *Ann Neurol* 1987; 21: 71–77.
28. Goodman AD, Brown TR, Krupp LB, et al. Sustained-release oral fampridine in multiple sclerosis: a randomised, double-blind, controlled trial. *Lancet* 2009; 373: 732–738.
29. Hayes KC, Blight AR, Potter PJ, et al. Preclinical trial of 4-aminopyridine in patients with chronic spinal cord injury. *Paraplegia* 1993; 31: 216–224.
30. Simpson DM, Goldenberg J, Kasner S, et al. Dalfampridine in chronic sensorimotor deficits after ischemic stroke: a proof of concept study. *J Rehabil Med* 2015; 47: 924–931.
31. Brugarolas P, Sanchez-Rodriguez JE, Tsai HM, et al. Development of a PET radioligand for potassium channels to image CNS demyelination. *Sci Rep* 2018; 8: 607.
32. Rodriguez-Rangel S, Bravin AD, Ramos-Torres KM, et al. Structure-activity relationship studies of four novel 4-aminopyridine K^+ channel blockers. *Sci Rep* 2020; 10: 52.
33. Fehlings MG and Nashmi R. Changes in pharmacological sensitivity of the spinal cord to potassium channel blockers following acute spinal cord injury. *Brain Res* 1996; 736: 135–145.
34. Brugarolas P, Reich DS and Popko B. Detecting demyelination by PET: the lesion as imaging target. *Mol Imaging* 2018; 17: 1536012118785471.
35. Basuli F, Zhang X, Brugarolas P, et al. An efficient new method for the synthesis of 3-[^{18}F]fluoro-4-Aminopyridine via Yamada-Curtius rearrangement. *J Labelled Comp Radiopharm* 2018; 61: 112–117.
36. Brugarolas P, Freifelder R, Cheng S-H, et al. Synthesis of meta-substituted [^{18}F]3-fluoro-4-aminopyridine via direct radiofluorination of pyridine N-oxides. *Chem Commun* 2016; 52: 7150–7152.
37. Brugarolas P, Bhuiyan M, Kucharski A, et al. Automated radiochemical synthesis of [^{18}F]3F4AP: a novel PET tracer for imaging demyelinating diseases. *J Vis Exp* 2017; 123: e55537.
38. Franklin RJ and Gallo V. The translational biology of remyelination: past, present, and future. *Glia* 2014; 62: 1905–1915.
39. Pike VW. PET radiotracers: crossing the blood-brain barrier and surviving metabolism. *Trends Pharmacol Sci* 2009; 30: 431–440.

40. Besnard J, Ruda GF, Setola V, et al. Automated design of ligands to polypharmacological profiles. *Nature* 2012; 492: 215–220.
41. Solingapuram Sai KK, Gage D, Nader M, et al. Improved automated radiosynthesis of [^{11}C]PBR28. *Sci Pharm* 2015; 83: 413–427.
42. Wilson AA, Garcia A, Chestakova A, et al. A rapid one-step radiosynthesis of the β-amyloid imaging radiotracer N-methyl-[^{11}C]2-(4′-methylaminophenyl)-6-hydroxybenzothiazole ([^{11}C]-6-OH-BTA-1). *J Labelled Cpd Radiopharm* 2004; 47: 679–682.
43. Richards ML and Scott PJH. Chapter 1: synthesis of [18F]-fluorodeoxyglucose ([^{18}F]FDG). In: Scott PJH and Hockley BG (eds). *Radiochemical syntheses volume I: radiopharmaceuticals for positron emission tomography*. Hoboken, NJ: John Wiley and Sons, Inc, 2012, pp.1–13.
44. Hilton J, Yokoi F, Dannals RF, et al. Column-switching HPLC for the analysis of plasma in PET imaging studies. *Nucl Med Biol* 2000; 27: 627–630.
45. Collier T, Normandin M, El Fakhri G, et al. Automation of column-switching HPLC for analysis of radiopharmaceuticals and their metabolites in plasma. *Soc Nucl Med Annual Meet Abstracts* 2013; 54: 1133.
46. Jenkinson M, Beckmann CF, Behrens TE, et al. Fsl. *Neuroimage* 2012; 62: 782–790.
47. Seidlitz J, Sponheim C, Glen D, et al. A population MRI brain template and analysis tools for the macaque. *Neuroimage* 2018; 170: 121–131.
48. Innis RB, Cunningham VJ, Delforge J, et al. Consensus nomenclature for in vivo imaging of reversibly binding radioligands. *J Cereb Blood Flow Metab* 2007; 27: 1533–1539.
49. Logan J, Fowler JS, Volkow ND, et al. Graphical analysis of reversible radioligand binding from time-activity measurements applied to [N-^{11}C-methyl]-(-)-cocaine PET studies in human subjects. *J Cereb Blood Flow Metab* 1990; 10: 740–747.
50. Ichise M, Toyama H, Innis RB, et al. Strategies to improve neuroreceptor parameter estimation by linear regression analysis. *J Cereb Blood Flow Metab* 2002; 22: 1271–1281.
51. Quinn B, Dauer Z, Pandit-Taskar N, et al. Radiation dosimetry of ^{18}F-FDG PET/CT: incorporating exam-specific parameters in dose estimates. *BMC Med Imaging* 2016; 16: 41.
52. Akaike H. A new look at the statistical model identification. *IEEE Trans Automat Contr* 1974; 19: 716–723.
53. Schafer EW, Jr., Brunton RB and Cunningham DJ. A summary of the acute toxicity of 4-aminopyridine to birds and mammals. *Toxicol Applied Pharmacol* 1973; 26: 532–538.
54. Imaizumi M, Briard E, Zoghbi SS, et al. Brain and whole-body imaging in nonhuman primates of [^{11}C]PBR28, a promising PET radioligand for peripheral benzodiazepine receptors. *Neuroimage* 2008; 39: 1289–1298.
55. Fujita M, Imaizumi M, Zoghbi SS, et al. Kinetic analysis in healthy humans of a novel positron emission tomography radioligand to image the peripheral benzodiazepine receptor, a potential biomarker for inflammation. *Neuroimage* 2008; 40: 43–52.
56. Stankoff B, Freeman L, Aigrot MS, et al. Imaging Central nervous system myelin by positron emission tomography in multiple sclerosis using [methyl-^{11}C]-2-(4'-methylaminophenyl)-6-hydroxybenzothiazole. *Ann Neurol* 2011; 69: 673–680.
57. Carvalho RHF, Real CC, Cinini S, et al. ^{11}C]PIB PET imaging can detect white and grey matter demyelination in a non-human primate model of progressive multiple sclerosis. *Mult Scler Relat Disord* 2019; 35: 108–115.
58. Sperling RA, Laviolette PS, O'Keefe K, et al. Amyloid deposition is associated with impaired default network function in older persons without dementia. *Neuron* 2009; 63: 178–188.
59. Paty DW. Magnetic resonance in multiple sclerosis. *Curr Opin Neurol Neurosurg* 1993; 6: 202–208.
60. Noseworthy JH, Paty DW and Ebers GC. Neuroimaging in multiple sclerosis. *Neurol Clin* 1984; 2: 759–777.
61. Bakshi R, Thompson AJ, Rocca MA, et al. MRI in multiple sclerosis: current status and future prospects. *Lancet Neurol* 2008; 7: 615–625.
62. Mihaly A, Toth G, Szente M, et al. Neocortical cytopathology in focal aminopyridine seizures as related to the intracortical diffusion of [^{3}H]4-aminopyridine. Electrophysiologic and light-microscopic studies. *Acta Neuropathol* 1985; 66: 145–154.
63. Armstrong CM and Loboda A. A model for 4-aminopyridine action on K^+ channels: similarities to tetraethylammonium ion action. *Biophys J* 2001; 81: 895–904.
64. Grossman RI, Gomori JM, Ramer KN, et al. Magnetization transfer: theory and clinical applications in neuroradiology. *Radiographics* 1994; 14: 279–290.
65. Rus H, Pardo CA, Hu L, et al. The voltage-gated potassium channel $K_v1.3$ is highly expressed on inflammatory infiltrates in multiple sclerosis brain. *Proc Natl Acad Sci U S A* 2005; 102: 11094–11099.